Effective extreme viscosity anisotropy enables environment-adaptive and geometry-arbitrary hydrodynamic metamaterials

Fubao Yang,[1,2,*] Yuhong Zhou,[3,*] Peng Jin,[3] Jinrong Liu,[1] Zhixin Li,[3] Lili Zhang,[3] Gaole Dai,[4,†] Liujun Xu,[2,‡] and Jiping Huang[3,§]

[1]*School of Physics, Faculty of Basic Sciences, University of Shanghai for Science and Technology, Shanghai 200093, China*

[2]*Graduate School of China Academy of Engineering Physics, Beijing 100193, China*

[3]*Department of Physics, State Key Laboratory of Surface Physics, and Key Laboratory of Micro and Nano Photonic Structures (MOE), Fudan University, Shanghai 200438, China*

[4]*School of Physical Science and Technology, Nantong University, Nantong 226019, China*

(Received 23 June 2025; accepted 22 May 2026; published 22 June 2026)

Hydrodynamic metamaterials offer novel strategies for liquid control, enabling local regulation of flow without disturbing the background field. However, existing passive designs are typically constrained by fixed working environments and regular geometries, which severely limit their applicability in complex scenarios. Here, we demonstrate a hydrodynamic metadevice that features both environment-adaptive and geometry-arbitrary properties. These unique capabilities arise from exploiting extreme viscosity anisotropy in Hele-Shaw flows, which can be effectively achieved through the structural design of microchannels. Numerical simulations and experiments verify that our metadevice with arbitrary geometry robustly preserves the background flow while increasing the central velocity, even under varying environmental conditions. This design framework extends the flexibility and robustness of hydrodynamic metamaterials for complex and dynamic environments, laying the groundwork for advanced microfluidic control.

DOI: 10.1103/7r2w-vzyj

I. INTRODUCTION

Liquid control is essential in diverse applications ranging from drug delivery to biomedical engineering [1,2]. These fields often require devices to maintain robust flow manipulation performance in the presence of environmental variations. Metamaterials, such as artificially engineered materials, have emerged as promising candidates for achieving unprecedented levels of field control [3–5], representing a significant technological advance with broad impact. In particular, hydrodynamic metamaterials have enabled remarkable control over liquid in recent years [6–21]. In regimes of low Reynolds number and confined flow conditions, commonly found in microfluidic systems [22], simplified models such as Darcy's law and the Hele-Shaw equation can be derived from the Navier-Stokes equations [23], providing a theoretical foundation for the design of hydrodynamic metamaterials. Based on transformation theory [24,25] and scattering cancellation technology [26–28], a variety of functional hydrodynamic metamaterials have been realized, including cloaks [10,11], concentrators [12], rotators [13], and multifunctional switches [14,15]. These metadevices

*These authors contributed equally to this work.
†Contact author: gldai@ntu.edu.cn
‡Contact author: ljxu@gscaep.ac.cn
§Contact author: jphuang@fudan.edu.cn

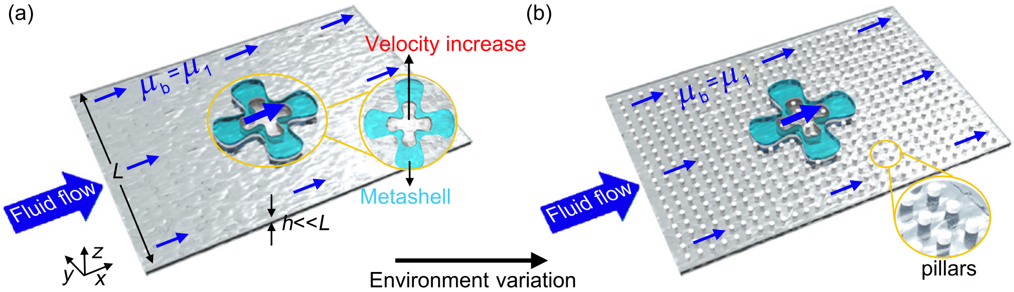

FIG. 1. (a), (b) Schematic illustration of the hydrodynamic concentrator in Hele-Shaw cells with different environments. The viscosity of the background liquid in (a) is $\mu_{\rm b} = \mu_1$. Uniformly arranged pillars are added to the background in (b) to produce environment variation, causing the effective background viscosity $\mu_{\rm b}$ to change from μ_1 to μ_2. The metashell viscosity satisfies $\mu_{\rm s} = {\rm diag}(0, \infty)$. The length and height of the cell are L and h, satisfying $h \ll L$. Blue arrows show the flow direction.

exhibit the remarkable ability to control flow within target regions while preserving the background flow field. The "invisibility" property makes hydrodynamic metamaterials particularly valuable in applications requiring high precision and stability.

Despite the rapid advances in hydrodynamic metamaterials, relative to the maturity achieved in electromagnetic and thermal domains [29–32], the field remains in its early stages and faces substantial challenges. Specifically, the development of self-adaptive hydrodynamic metamaterials that can respond to changing environmental conditions is crucial for enabling new levels of adaptability and efficiency [33]. However, due to the lack of an effective design strategy, existing passive hydrodynamic metamaterials are typically designed for specific environments and regular geometries. As a result, variations in environmental conditions or device geometry often compromise their invisibility and distort the surrounding flow, thereby limiting their applicability to complex and dynamically changing real-world scenarios. Overcoming limitations in environmental adaptability and geometric freedom thus represents an essential step forward for the field. Active control strategies [15] have been introduced to enable adaptability, but they are generally limited to regular geometries and involve external energy input. Alternative approaches have explored the use of extremely anisotropic parameters to impart adaptability to metashells [34–38]. However, the attainable viscosity anisotropy ratio is fundamentally constrained by the lack of long-range order in most liquids. Consequently, the experimental realization of such extreme viscosity anisotropy in hydrodynamic metamaterials remains elusive.

In this work, we present a theoretical approach and an experimental demonstration of hydrodynamic metadevices that exhibit both environment-adaptive and geometry-arbitrary properties by harnessing extreme viscosity anisotropy. We show that hydrodynamic systems provide a physically accessible route to effectively realizing extreme viscosity anisotropy. Environmental variation is examined here in two representative ways: by varying the effective background viscosity in the 2D theory and simulations, and by modifying the background structure in the 3D simulations and experiments. Our device operates within a Hele-Shaw cell [23], which describes Stokes flow between two parallel plates separated by a gap much smaller than their lateral dimensions. A schematic of the device is shown in Fig. 1(a). To highlight the geometric freedom, we employ a metashell with a four-leaf clover shape. This metashell, endowed with extreme viscosity anisotropy, can maintain invisibility under varying environmental conditions [Fig. 1(b)], demonstrating an environmental adaptability not achievable by existing passive hydrodynamic metamaterials. Furthermore, due to the extreme viscosity anisotropy, the metashell acts as a flow concentrator, significantly enhancing the pressure gradient and flow velocity in the core region. While realizing extreme viscosity anisotropy in practice is generally challenging, we achieve it equivalently by modulating the liquid

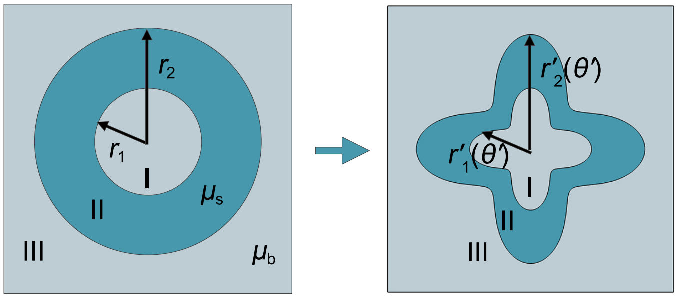

FIG. 2. Diagram of a radial coordinate transformation that transforms a circular shell into an irregularly shaped shell.

heights in different regions of the metashell, leveraging the principle of communicating vessels. The effectiveness of our approach is validated through both simulations and experiments. The proposed hydrodynamic metadevice offers enhanced adaptability and robustness, ensuring reliable performance even in complex and dynamically changing environments.

II. THEORETICAL FRAMEWORK

The environment-adaptive and geometry-arbitrary properties of the metashell originate from its extreme viscosity anisotropy. We consider an incompressible creeping flow in a Hele-Shaw cell with width L and height h. The average velocity $\overline{\boldsymbol{v}}$ in the x-y plane satisfies [23]

$$\overline{\boldsymbol{v}} = \frac{-h^2}{12\mu}\boldsymbol{\nabla}P, \tag{1}$$

where μ is the viscosity of the liquid, and $\boldsymbol{\nabla}P$ is the applied pressure bias. $\overline{\boldsymbol{v}}$ is taken as the velocity $\boldsymbol{v}$ in this model. Considering the law of continuity $\boldsymbol{\nabla}\cdot(h\boldsymbol{v}) = 0$, we obtain the following governing equation:

$$\boldsymbol{\nabla}\cdot(\gamma\boldsymbol{\nabla}P) = 0, \tag{2}$$

where $\gamma = h^3/12\mu$. Equation (2) shows that the flow field can be controlled by modulating the viscosity.

We first demonstrate the environmental adaptability induced by extreme viscosity anisotropy. The model is simplified to a two-dimensional scenario, as shown in Fig. 2. The entire system is divided into three regions. Region I (core) and region III represent the background, both with the same viscosity μ_{b}, which denotes the effective viscosity of the liquid in the background and may vary depending on the liquid type or environmental structure. Region II (shell) constitutes the metashell, characterized by an extremely anisotropic viscosity tensor $\boldsymbol{\mu}_{\mathrm{s}} = \mathrm{diag}(\mu_{\mathrm{r}}, \mu_{\theta}) = \mathrm{diag}(0, \infty)$. By directly solving Eq. (2) (see Appendix A 1 for details), we derive the effective viscosity μ_{e} of the core-shell region (regions I and II) as

$$\mu_{\mathrm{e}} = \frac{\mu_{\mathrm{r}}}{m}\frac{(1-p^m)\mu_{\mathrm{r}} + (1+p^m)m\mu_{\mathrm{b}}}{(1+p^m)\mu_{\mathrm{r}} + (1-p^m)m\mu_{\mathrm{b}}}, \tag{3}$$

where $m = \sqrt{\mu_{\mathrm{r}}/\mu_{\theta}}$ and $p = (r_1/r_2)^2$. Here, r_1 and r_2 denote the inner and outer radii of the shell, respectively. Substituting $\mu_{\mathrm{r}} = 0$ and $\mu_{\theta} = \infty$ into Eq. (3), we obtain $\mu_{\mathrm{e}} = \mu_{\mathrm{b}}$. This result indicates that the metashell exhibits environmentally adaptive behavior: regardless of variations in the background viscosity μ_{b}, the metashell adapts and preserves the invisibility property. Due to its extreme viscosity anisotropy, the metashell functions as a perfect concentrator.

We further demonstrate its geometric freedom. Equation (2) satisfies transformation theory. Considering an original space (r, θ) and a transformed space (r', θ'), the transformation rule is given by $\boldsymbol{\gamma}' = \mathbf{J}\boldsymbol{\gamma}\mathbf{J}^{\mathrm{T}}/\det\mathbf{J}$, where $\boldsymbol{\gamma}'$ and $\boldsymbol{\gamma}$ are the parameters in the transformed and original spaces, respectively. $\mathbf{J}$ is the Jacobian matrix, expressed as $\mathbf{J} = \partial(r', \theta')/\partial(r, \theta)$, and $\mathbf{J}^{\mathrm{T}}$ denotes its transpose. For the case of modulating viscosity, the transformation rule can be expressed as $\boldsymbol{\mu}' = \det\mathbf{J}(\mathbf{J}^{\mathrm{T}})^{-1}\boldsymbol{\mu}\mathbf{J}^{-1}$. We then consider a radial coordinate transformation $r' = F(r, \theta)$ and $\theta' = \theta$ to transform the circular shell [with $\boldsymbol{\mu}_{\mathrm{s}} = \mathrm{diag}(0, \infty)$] into an irregularly shaped shell [Fig. 1(a)]. The transformed viscosity tensor of the metashell $\boldsymbol{\mu}'_{\mathrm{s}}$ satisfies

$$\boldsymbol{\mu}'_{\mathrm{s}} = \begin{bmatrix} \mu_{11} & \mu_{12} \\ \mu_{21} & \mu_{22} \end{bmatrix}, \tag{4}$$

where $\mu_{11} = 0$, $\mu_{12} = \mu_{21}$ are finite values, $\mu_{22} = \infty$, and $\Delta \equiv \det\boldsymbol{\mu}'_{\mathrm{s}} = \mu_{11}\mu_{22} - \mu_{12}^2 > 0$ (see Appendix A 2 for details). Substituting Eq. (4) into Eq. (2), we have

$$\frac{1}{r}\frac{\partial}{\partial r}\left[r\left(\frac{\mu_{22}}{\Delta}\frac{\partial P}{\partial r} - \frac{\mu_{12}}{\Delta}\frac{\partial P}{r\partial\theta}\right)\right] + \frac{1}{r}\frac{\partial}{\partial\theta}\left[-\frac{\mu_{12}}{\Delta}\frac{\partial P}{\partial r} + \frac{\mu_{11}}{\Delta}\frac{\partial P}{r\partial\theta}\right] = 0. \tag{5}$$

μ_{12} and μ_{21} have negligible effects on transport and can thus be omitted. By setting them to zero, we obtain

$$\boldsymbol{\mu}'_{\mathrm{s}} = \mathrm{diag}(0, \infty). \tag{6}$$

The theoretical analysis indicates that metashells with extreme viscosity anisotropy exhibit environment-adaptive and geometry-arbitrary properties. Similar conclusions can also be drawn from the perspective of a null medium [39–42]. The detailed derivation is provided in Appendix A 3.

III. TWO-DIMENSIONAL NUMERICAL SIMULATION

We performed two-dimensional (2D) finite-element simulations to evaluate the performance of a hydrodynamic metashell with extreme viscosity anisotropy. The simulated model has dimensions 30 cm $\times$ 20 cm. The left and right boundaries are set to 40 and 0 Pa, respectively, while no-slip conditions are imposed on the top and bottom boundaries. A liquid with viscosity $\mu_{\mathrm{f}} = 0.001$ Pa s (approximating water) is selected as the reference liquid, and different background viscosities μ_{b} are set relative to this value. We evaluate the metashell in viscous backgrounds with $\mu_{\mathrm{b}} = \mu_{\mathrm{f}}$, $10\mu_{\mathrm{f}}$, and $0.1\mu_{\mathrm{f}}$, respectively, to assess its environmental adaptability. The pressure and velocity field distributions are shown in Figs. 3(a)–3(c) and Figs. 3(f)–3(h), respectively. The fields in region III remain undisturbed under different viscous backgrounds, exhibiting invisibility. Meanwhile, the pressure gradient and velocity in region I are enhanced, demonstrating a concentrating effect.

For quantitative accuracy analysis, we extract the pressure distribution along the outer contour of the metashell under three different background viscosities and plot the results in Fig. 3(d). The three sets of data coincide, demonstrating the validity of the theoretical predictions. To evaluate the influence of the metashell on region III, we use a pure background (without the metashell) as the reference group. By subtracting the reference group's pressure from that of $\mu_{\mathrm{b}} = \mu_{\mathrm{f}}$ in Fig. 3(a) across the entire domain, we obtain the pressure difference, shown in Fig. 3(e). The red dots represent these differences and are nearly zero in region III, indicating that the metashell has a negligible impact on this region. To quantitatively evaluate the metashell's influence on the velocity field, we extract velocity data along four horizontal lines at $y = 0, 3, 6, 9$ cm, and we subtract the corresponding reference group data from each line. The results are illustrated in Figs. 3(i)–3(k). It is observed that the velocity difference between the metashell (v_{m}) and the reference background (v_{r}) is zero ($\Delta v = v_{\mathrm{m}} - v_{\mathrm{r}} = 0$) in region III. This confirms that the metashell has no impact on the background velocity field. The detailed velocity distributions and their exact differences are provided in Appendix B 1. Moreover, the metashell retains its environmental adaptability even when its geometry is asymmetric (see Fig. 4), demonstrating the robustness of the theoretical model.

To highlight the fundamental difference between our proposed design and conventional approaches, it is instructive to compare our method with a standard design paradigm, which we

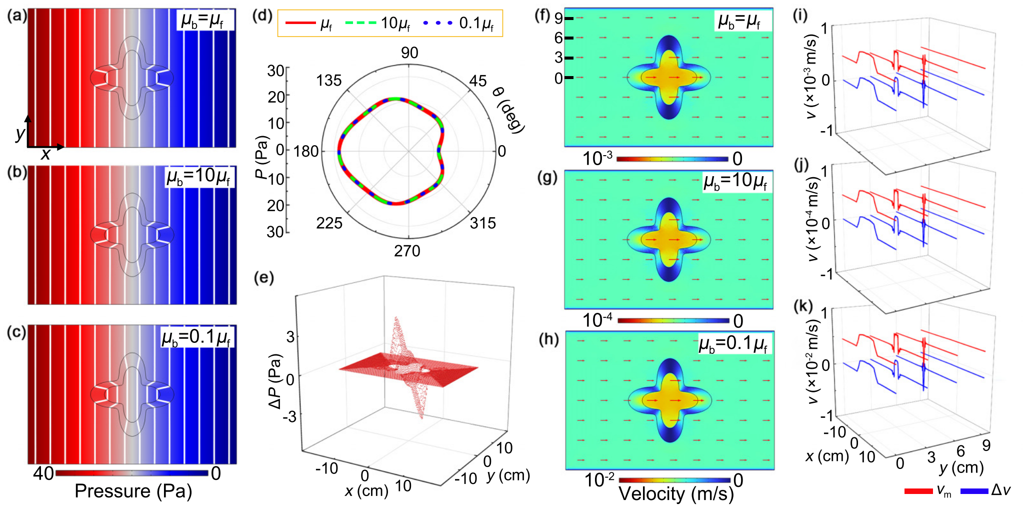

FIG. 3. 2D simulation results of the metashell. (a)–(c) Pressure distributions for $\mu_\mathrm{b} = \mu_\mathrm{f}$, $10\mu_\mathrm{f}$, and $0.1\mu_\mathrm{f}$, respectively, with white lines representing isobars. (d) Angular pressure profiles along the outer contour for the three cases: $\mu_\mathrm{b} = \mu_\mathrm{f}$ (red solid), $10\mu_\mathrm{f}$ (green dashed), and $0.1\mu_\mathrm{f}$ (blue dotted). (e) Pressure differences between the metashell and the reference on the xy-plane for $\mu_\mathrm{b} = \mu_\mathrm{f}$. (f)–(h) Corresponding velocity distributions, with red arrows denoting normalized velocity vectors. (i)–(k) Corresponding velocity profiles along four lines ($y = 0, 3, 6, 9$ cm). Red lines denote the metashell velocity (v_m), and blue lines indicate the difference from the reference ($\Delta v = v_\mathrm{m} - v_\mathrm{r}$). The irregular metashell boundaries are defined by $r_1(\theta) = \cos(4\theta) + 3$ cm and $r_2(\theta) = 1.5[\cos(4\theta) + 3]$ cm, with a viscosity tensor $\boldsymbol{\mu} = \mathrm{diag}(10^{-3}\mu_\mathrm{f},\ 10^{3}\mu_\mathrm{f})$.

term the normal transformed shell (NTS). In the traditional transformation framework, the required effective viscosity tensor of the shell is derived by directly mapping a predefined, uniform background. Consequently, the theoretical parameters of the NTS are coupled with a specific background viscosity. If the background environment changes, this predefined parameter modulation can no longer satisfy the transformation requirements. As shown in Figs. 5(a)–5(c) and 5(g)–5(i), an NTS designed for a specific reference background ($\mu_\mathrm{b} = \mu_\mathrm{f}$) performs well only under that exact condition. When the background viscosity varies (e.g., to $\mu_\mathrm{b} = 0.1\mu_\mathrm{f}$ or $10\mu_\mathrm{f}$), the mismatch between the fixed NTS parameters and the new background inevitably causes flow distortion. In contrast, our proposed extremely anisotropic shell (EAS) introduces a different mechanism, as it is governed by

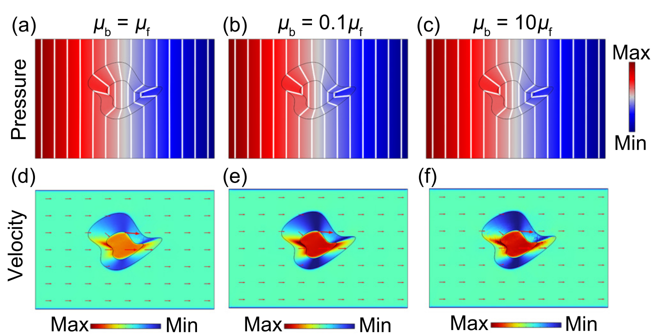

FIG. 4. 2D simulation results of the metashell with asymmetric geometry. (a)–(c) Simulation results of pressure distributions when $\mu_\mathrm{b} = \mu_\mathrm{f}$, $10\mu_\mathrm{f}$, and $0.1\mu_\mathrm{f}$, respectively. (d)–(f) Corresponding velocity distributions. The parameters are the same as in Fig. 3.

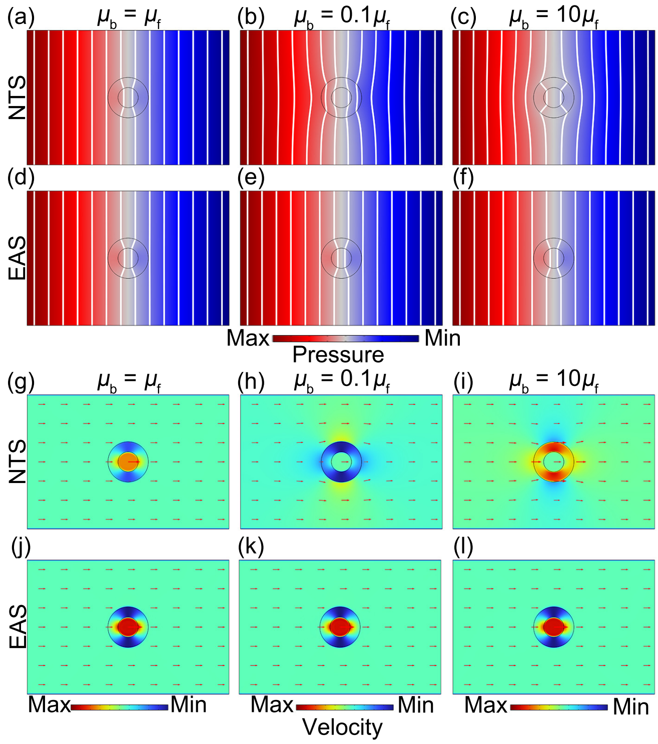

FIG. 5. Performance differences between the extremely anisotropic shell (EAS) and the normal transformed shell (NTS). (a)–(c) Pressure distributions of the NTS under three different viscosity backgrounds. (d)–(f) Pressure distributions of the EAS under three different viscosity backgrounds. (g)–(l) Corresponding velocity distributions.

an extremely anisotropic viscosity tensor. Under this condition, the effective background viscosity mathematically cancels out of the governing equations. This decoupling allows the EAS to maintain its desired performance across diverse environmental conditions, as shown in Figs. 5(d)–5(f) and 5(j)–5(l).

IV. THREE-DIMENSIONAL NUMERICAL SIMULATION

In our design, the extreme effective viscosity tensor $\boldsymbol{\mu}'_{\mathrm{s}} = \mathrm{diag}(0, \infty)$ is physically realized through a tailored microchannel architecture. The condition $\mu_\theta \to \infty$ is implemented by introducing solid barriers to prevent tangential flow. For the radial component, the mapping between effective viscosity and structural geometry is governed by the Hele-Shaw flow conductance, defined as $\gamma = h^3/(12\mu)$. According to this relation, the channel height h and the intrinsic viscosity μ have inverse effects on transport. Therefore, by increasing the height h of the radial liquid channels within the metashell, the local flow resistance is reduced. This geometric modulation allows the liquid to propagate radially with a vanishing pressure gradient ($\nabla_r P \approx 0$) while maintaining a continuous macroscopic flow ($v_r \neq 0$). This geometrically induced isobaric condition is equivalent to an effective radial viscosity approaching zero ($\mu_r \to 0$). Combining solid barriers with heightened radial channels yields the required extreme effective viscosity tensor, $\boldsymbol{\mu}'_{\mathrm{s}} = \mathrm{diag}(0, \infty)$.

We perform three-dimensional simulations to evaluate the structural design, as illustrated in Fig. 6. Liquid regions are shown in color, while blank areas correspond to solid-occupied regions. The model has dimensions of 20 cm $\times$ 30 cm, with a height of 0.02 cm in the background and 0.2 cm

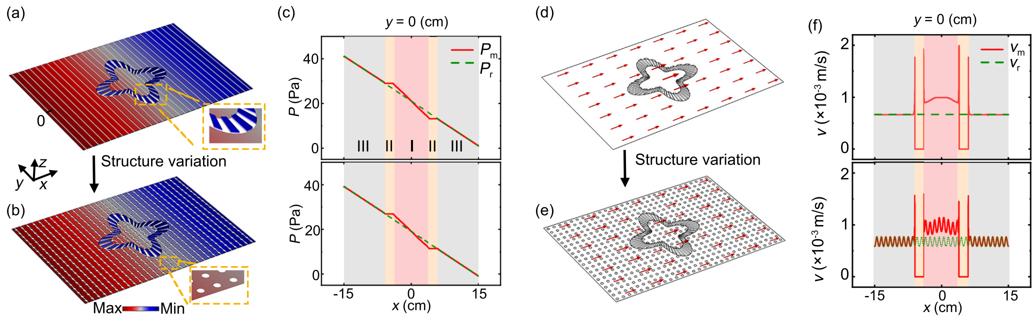

FIG. 6. 3D simulation results of the metashell. (a), (b) Pressure distributions of the metashell under two different backgrounds. The boundary conditions are the same as in the 2D case. (c) Pressure data plots for the metashell (P_{m}) compared to reference groups (P_{r}) along the $y = 0\,\mathrm{cm}$ line at the $z = 0.01\,\mathrm{cm}$ plane. (d), (e) Corresponding velocity distributions. (f) Velocity data plots for the metashell (v_{m}) compared to reference groups (v_{r}) along the $y = 0\,\mathrm{cm}$ line at the $z = 0.01\,\mathrm{cm}$ plane.

in the metashell. A reference liquid with viscosity $\mu_{\mathrm{f}} = 0.001\,\mathrm{Pa\,s}$ is used. The geometry matches the 2D case. Figure 6(a) is the pressure distribution. The straight isobars confirm the accuracy of our design. To assess the metashell's environmental adaptability, we alter the background structure rather than the liquid, as shown in Fig. 6(b). Uniformly arranged pillars (radius: 0.2 cm) are added to the background to effectively change viscosity. The straight isobars indicate that the metashell remains invisible, demonstrating its adaptability to environmental structural variations. Figure 6(c) quantitatively displays the pressure distributions for two different backgrounds, and compares them to those of the reference groups—uniform backgrounds without the metashell. In both cases, the metashell region is nearly isobaric, and the pressure in region III matches well with the reference data. Additionally, the pressure gradient in region I exceeds that in region III, indicating a concentration effect. The corresponding velocity distributions [Figs. 6(d) and 6(e)] further confirm the environmental adaptability, and also demonstrate both the invisibility and acceleration effects in the velocity field [Fig. 6(f)]. Detailed quantitative analyses are provided in Appendix B 2. However, if the metashell consisted solely of isobaric regions, rather than alternating structures, it would disturb the background field (see Appendix B 3).

V. EXPERIMENTAL VALIDATION

Furthermore, we conduct experiments. The experimental setup [Fig. 7(a)] replicates the simulated model with dimensions $20\,\mathrm{cm} \times 30\,\mathrm{cm} \times 0.1\,\mathrm{cm}$. A fully filled reservoir provides the desired high-pressure condition, with liquid flowing out from the opposite end. In the metashell, high-viscosity regions are sealed with solid, while low-viscosity, isobaric regions are implemented via the principle of communicating vessels, allowing the liquid surface to rise and approximate ideal isobaric conditions. This is realized by mounting a structured solid cap: hollowed above isobaric regions, solid elsewhere [exploded view in Fig. 7(a)]. We use dye injection, a common method for flow visualization in hydrodynamic metamaterials, to characterize the performance of our metashell. Glycerin ($\mu = 0.63\,\mathrm{Pa\,s}$) is used to ensure creeping flow, visualized with colored ink. The ink pattern is recorded from beneath the setup. To test the environmental adaptability, we fabricated two experimental setups, as shown in Figs. 7(b) and 7(c). The setup in Fig. 7(c) builds upon that of Fig. 7(b) by adding periodically arranged pillars in regions I and III. Detailed experimental procedures are provided in Appendix C1.

The experimental results, as shown in Figs. 7(d) and 7(e), indicate that the ink streamlines in region III remain straight under both background configurations, thereby verifying the metashell's adaptability and geometric freedom. A quantitative evaluation of the streamline straightness is

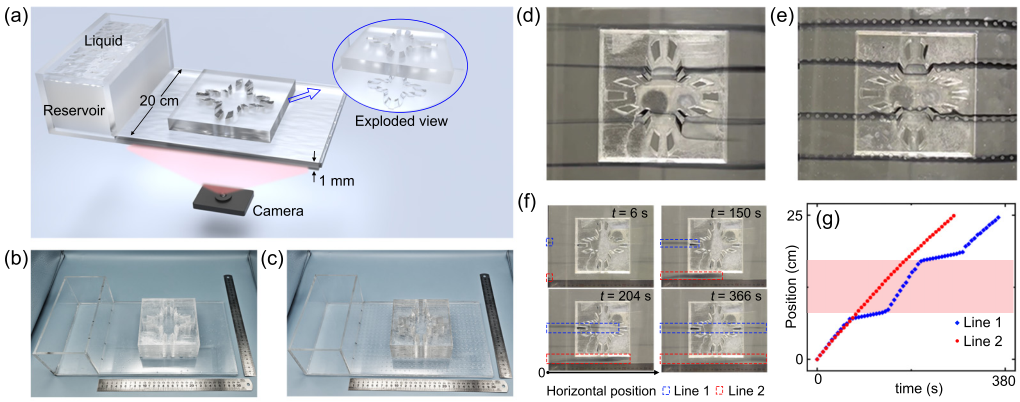

FIG. 7. Experimental validation of the metashell. (a) Schematic diagram of the setup. (b) Experimental setup. (c) Modified setup with periodically arranged pillars to equivalently adjust the background viscosity. (d), (e) Photographs of the experimental results for two setups. Black lines indicate ink trails. (f) Two representative streamlines passing through the core and the background at four time points. (g) The horizontal position of the leading edge of the ink fronts along two streamlines over time.

provided in Appendix C 2. To further confirm the robustness of our observations, additional experiments were conducted by increasing the tracked streamlines from four to seven (see Appendix C 3). Furthermore, to verify the acceleration effect in the core region, we tracked the horizontal position of the leading edge of the ink fronts over time along two representative streamlines passing through the core and the background, respectively. Figure 7(f) shows two representative streamlines at four time points. Figure 7(g) presents the resulting position-time scatter plot. The pink shaded region corresponds to the horizontal range of the core region. As observed, within this zone, the slope of line 1 is steeper than that of line 2, quantitatively confirming that the velocity is higher and accelerated in the core. In contrast, outside the core region, the identical slopes of lines 1 and 2 confirm that the background velocity magnitude is conserved. These results demonstrate that the spatial pressure and velocity fields in the background region remain undisturbed. However, as visually observed in the experimental ink fronts, the liquid trajectories experience a cumulative time delay compared to the background. Because the shell region utilizes an enlarged channel height to equivalently achieve $\mu_{\mathrm{r}} \rightarrow 0$, the continuity equation dictates that the velocity decreases in this zone. This temporal delay can be mitigated in practice by minimizing the radial thickness of the metashell.

VI. EXTENDED APPLICABILITY

In addition to being adaptive to variations in viscosity, our metashell also exhibits omnidirectionality, meaning it remains effective even when the direction of the background flow field changes. This property is fundamentally guaranteed by transformation theory, which dictates the required extreme anisotropic viscosity. To verify this, we simulated the 2D metashell rotated by 30° and 45° relative to the flow. As shown in Figs. 8(a) and 8(b), the unperturbed background fields are robustly maintained. Furthermore, 3D simulations of the structure [from Fig. 6(a)] rotated by 45° demonstrate nearly identical pressure and velocity fields compared to the reference [Figs. 8(c) and 8(d)]. Quantitatively, the polar pressure distribution [Fig. 8(e)] and the velocity profile [Fig. 8(f)] of the metashell (P_{m}, v_{m}) and reference (P_{r}, v_{r}) almost overlap. The average pressure deviation at four representative background points [(0, ±3.5, 0.01) cm and (±3.5, 0, 0.01) cm] is merely ∼0.9%, confirming the robust omnidirectional cloaking capabilities of our design.

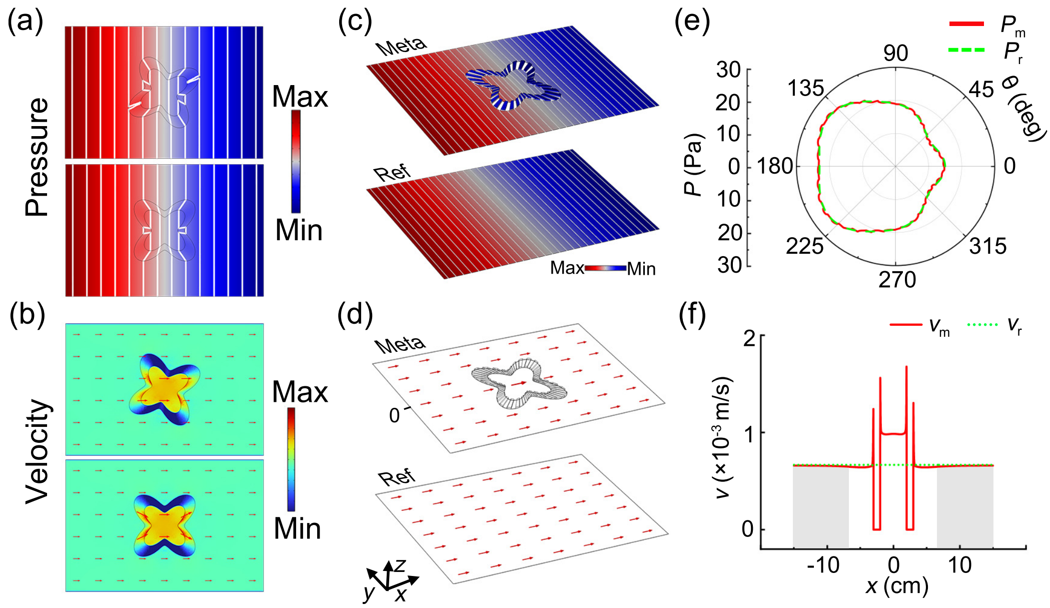

FIG. 8. Omnidirectional cloaking performance of the metashell. (a), (b) 2D simulation results. (a) Pressure and (b) velocity distributions when the metashell is rotated by 30° (top panels) and 45° (bottom panels) relative to the background flow. (c)–(f) 3D simulation results for the metashell rotated by 45°. (c) Pressure and (d) velocity fields comparing the metashell system (Meta, top) and the homogeneous reference system (Ref, bottom). Quantitative validations are provided by (e) the pressure profiles (P_{m} vs P_{r}) extracted along the outer contour of the shell and (f) the velocity profiles (v_{m} vs v_{r}) extracted along the line $y = 0$. Both profiles in (e) and (f) are evaluated at the $z = 0.01$ cm plane.

It is important to note that the validity of our design, based on the Hele-Shaw model, is contingent on the flow being in the low Reynolds number regime (Re $\ll 1$). The Reynolds number (Re $= \rho v l/\mu$, where ρ is the liquid density and l is the channel height) is the key parameter governing the flow physics, rather than velocity alone. All results presented in our main text correspond to Re < 0.2, where inertial effects are negligible and the metashell performs well, with average pressure deviation $(P_{\mathrm{m}} - P_{\mathrm{r}})/P_{\mathrm{r}}$ at four background points (± 3 cm, ± 3 cm, 0.01 cm) being around 1.2%. To explore the operational limits, we investigated the metashell's performance at higher Reynolds numbers. With liquid properties and structure dimensions fixed, increasing the velocity directly translates to increasing Re. We performed 3D simulations using a laminar flow module that incorporates full inertial terms. The structural geometry from Fig. 6 is used, and the corresponding results for Re $\rightarrow 1$, 10, 100, and 300 are detailed in Fig. 9.

For Re $\rightarrow 1$ [Figs. 9(a)–9(c)] and Re $\rightarrow 10$ [Figs. 9(d)–9(f)], the cloaking performance remains robust. The 3D pressure and velocity fields are nearly unperturbed. Quantitatively, the polar pressure profiles along the shell's outer contour (P_{m}) and the velocity profiles along the x-axis (v_{m}) match the homogeneous reference (P_{r}, v_{r}) closely. The calculated average pressure deviations at the aforementioned four background points are 1.1% and 1.3%, respectively. However, as Re further increases to 100 [Figs. 9(g)–9(i)] and 300 [Figs. 9(j)–9(l)], inertia becomes dominant. Visible disturbances begin to appear in the background fields, and the extracted pressure and velocity curves deviate from the reference lines, with average pressure deviations rising to 3.9% and 6.9%, respectively. These results indicate that while our metashell functions optimally in the creeping flow regime, its invisible performance remains acceptable up to Re ≈ 10. For fixed liquid properties and metashell geometry, the maximum operational velocity—and thus the upper limit of Re—can

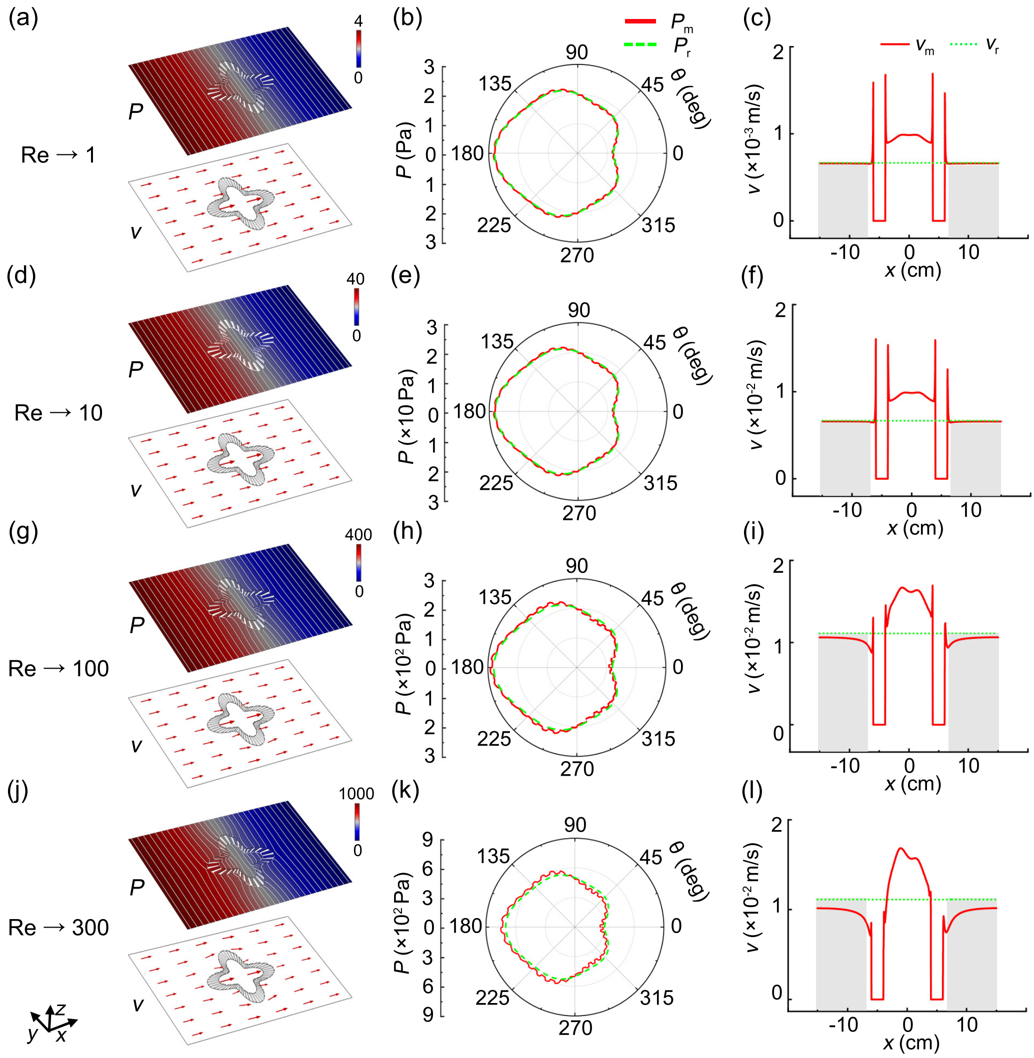

FIG. 9. Operational limits of the metashell at varying Reynolds numbers. 3D simulation results incorporating full inertial terms for (a)–(c) Re → 1, (d)–(f) Re → 10, (g)–(i) Re → 100, and (j)–(l) Re → 300. Left column [(a), (d), (g), (j)]: 3D background pressure (P) and velocity (v) fields. Middle column [(b), (e), (h), (k)]: Comparison of the polar pressure profiles (P_m vs P_r) extracted along the outer contour of the shell. Right column [(c), (f), (i), (l)]: Comparison of the velocity profiles (v_m vs v_r) extracted along the center line $y = 0$. Both profiles in the middle and right columns are evaluated at the $z = 0.01$ cm plane.

be determined based on the acceptable tolerance of background disturbance for specific practical applications.

Crucially, the underlying physical principles of our metashell are inherently scale-invariant. Its hydrodynamic performance is governed not by absolute physical dimensions, but by the dimensionless geometric aspect ratio (the Hele-Shaw requirement $h \ll L, W$) and the creeping flow condition ($\mathrm{Re} \ll 1$). To explicitly demonstrate this scalability, we performed additional 2D and 3D simulations of the metashell scaled down by factors of 5 and 10 (see Fig. 10). The simulated pressure and velocity fields quantitatively match those of the original design, confirming that the environment-adaptive cloaking functionalities are preserved at smaller scales.

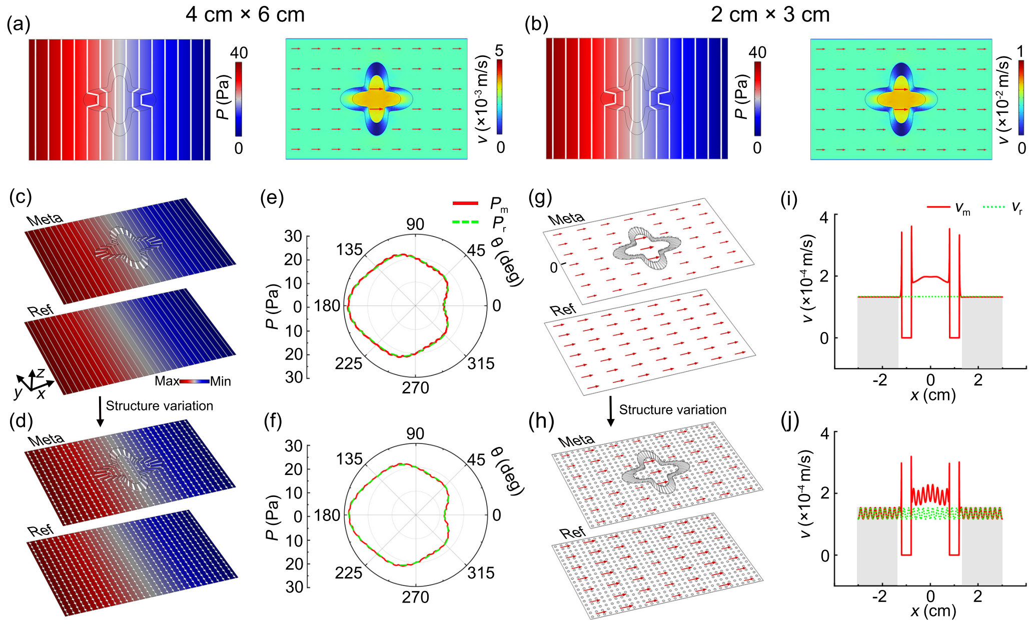

FIG. 10. Scalability of the metashell. (a),(b) 2D simulation results showing the pressure and velocity distributions after reducing the system size by (a) five times (4 cm × 6 cm) and (b) ten times (2 cm × 3 cm). (c)–(j) 3D simulation results for the metashell scaled down by five times (4 cm × 6 cm × 40 μm). (c)–(f) Pressure distributions and (g)–(j) corresponding velocity distributions comparing the metashell and the reference flow.

VII. CONCLUSION

In this work, we demonstrate a hydrodynamic metadevice that simultaneously exhibits environment-adaptive and geometry-arbitrary properties, enabled by the realization of extreme viscosity anisotropy using simple structural designs. Our theoretical framework based on the Hele-Shaw model accurately captures the metashell's adaptive behavior, as confirmed by finite-element simulations and experiments. While previous passive hydrodynamic cloaks successfully utilized microstructures, such as micropillars, to achieve anisotropic viscosity, these solid obstacles function by strictly increasing flow resistance, thereby generating finite and positive effective viscosities. Because such designs rely on finite effective parameters mathematically proportional to a specific background, their cloaking performance is inherently disrupted if the background environment changes. In contrast, our structural strategy utilizes height variations and solid barriers to physically realize an extreme effective viscosity tensor. As demonstrated above, this extreme condition mathematically decouples the device's performance from the background viscosity, enabling both environmental adaptability and geometric freedom.

Moreover, a key functional advantage of our design is its ability to selectively accelerate flow in the core region, while preserving the background flow. This velocity modulation allows for precise control over localized flow processes, which is helpful for advanced functionalities in microfluidic and laboratory-on-a-chip systems [43], with direct benefits for mixing, separation, and droplet generation [44]. The feasibility of deploying our design in such practical microfluidic systems is further guaranteed by its geometric scalability. Since the functionality relies on the relative height ratio (e.g., 10:1) rather than absolute dimensions, the structure can be proportionally scaled up to avoid fabrication challenges associated with excessively narrow channels. Potential applications of the metashell in accelerating liquid mixing within microfluidic chips, along with its robustness in handling liquids with different viscosities, are further discussed in Appendix D. Furthermore, we can explore the impact of varying liquid properties over a broader range. For instance, extending the design to non-Newtonian regimes [45–48] is a challenging but promising direction. Additionally, our model can be extended to multiphysics domains, provided that its key parameters conform to transformation theory and effective medium theory (e.g., thermal-hydrodynamic coupling [49–52]). Our approach offers a robust platform for flow control in complex environments, paving the way for advanced liquid manipulation across diverse scientific and engineering applications.

ACKNOWLEDGMENTS

J.H. gratefully acknowledged the support by the National Natural Science Foundation of China under Grant No. 12320101004, and the Innovation Program of the Shanghai Municipal Education Commission under Grant No. 2023ZKZD06. L.X. acknowledged the support by the National Natural Science Foundation of China under Grants No. 12375040 and No. 12088101, and the Science Challenge Project under Grant No. TZ2025017. G.D. acknowledged the support by the National Natural Science Foundation of China under Grant No. 12305046.

DATA AVAILABILITY

There are no publicly available research data or software supporting this manuscript. Requests for further information or data should be sent to the authors.

APPENDIX A: DETAILED THEORETICAL DERIVATIONS

1. Detailed derivations for the effective viscosity

The pressure fields in regions I, III, and the metashell are denoted as P_1, P_3, and P_s, respectively. The viscosity of the metashell satisfies $\boldsymbol{\mu}_s = \mathrm{diag}(\mu_r, \mu_\theta) = \mathrm{diag}(0, \infty)$. We use μ_1 and μ_3 to represent the viscosity in regions I and III, respectively. Since h is a constant, we replace γ with μ^{-1} and rewrite the Hele-Shaw equation as

$$\nabla \cdot (\mu^{-1} \nabla P) = 0. \tag{A1}$$

We solve Eq. (A1) directly in cylindrical coordinates. Thus, we have

$$\frac{1}{r}\partial_r\left(r\mu_r^{-1}\partial_r P\right) + \frac{1}{r}\partial_\theta\left(\frac{\mu_\theta^{-1}}{r}\partial_\theta P\right) = 0. \tag{A2}$$

The general solution to Eq. (A2) is

$$P = A_0 + B_0 \ln r + \sum_{i=1}^{\infty}[A_i \cos(i\theta) + B_i \sin(i\theta)]r^{im} + \sum_{j=1}^{\infty}[C_j \cos(j\theta) + D_j \sin(j\theta)]r^{-jm}, \tag{A3}$$

where $m = \sqrt{\mu_r/\mu_\theta}$. The constants $A_0, B_0, A_i, B_i, C_j, D_j$ are determined by the boundary conditions. Based on our theoretical design, the boundary conditions are given by

$$\begin{aligned} &P_1|_{r\to 0} \text{ is finite}, \quad P_1|_{r=r_1} = P_s|_{r=r_1}, \quad P_s|_{r=r_2} = P_3|_{r=r_2}, \quad -\mu_1^{-1}\partial_r P_1|_{r=r_1} = -\mu_r^{-1}\partial_r P_s|_{r=r_1}, \\ &-\mu_r^{-1}\partial_r P_s|_{r=r_2} = -\mu_3^{-1}\partial_r P_3|_{r=r_2}, \quad P_3|_{r\to\infty} = -\nabla P r \cos\theta. \end{aligned} \tag{A4}$$

Here, ∇P represents a uniform gradient field along the r-direction. Considering the symmetry of the boundary conditions, we obtain the following expressions for the pressure fields:

$$P_1 = A_0 + B_{11} r \cos\theta, \tag{A5a}$$

$$P_s = A_0 + B_{s1} r^m \cos\theta + C_{s1} r^{-m} \cos\theta, \tag{A5b}$$

$$P_3 = A_0 + B_{31} r \cos\theta + C_{31} r^{-1} \cos\theta. \tag{A5c}$$

Substituting Eqs. (A5a)–(A5c) into Eq. (A4), we obtain the following system of equations:

$$\begin{aligned}
B_{11}r_1 &= B_{s1}r_1^m + C_{s1}r_1^{-m},\\
B_{s1}r_2^m + C_{s1}r_2^{-m} &= B_{31}r_2 + C_{31}r_2^{-1},\\
\mu_1^{-1}B_{11} &= \mu_r^{-1}\left(mB_{s1}r_1^{m-1} - mC_{s1}r_1^{-m-1}\right),\\
\mu_r^{-1}\left(mB_{s1}r_2^{m-1} - mC_{s1}r_2^{-m-1}\right) &= \mu_3^{-1}\left(B_{31} - C_{31}r_2^{-2}\right),\\
B_{31} &= |\nabla P|.
\end{aligned} \tag{A6}$$

To ensure that the pressure field in region III is not disturbed, we set $C_{31} = 0$. Solving Eq. (A6), we obtain that the viscosity satisfies the following relation:

$$\mu_3 = \frac{\mu_r}{m}\frac{(1-p^m)\mu_r + (1+p^m)m\mu_1}{(1+p^m)\mu_r + (1-p^m)m\mu_1}. \tag{A7}$$

Letting $\mu_e = \mu_3$, we derive the effective viscosity of the core-shell structure as

$$\mu_e = \frac{\mu_r}{m}\frac{(1-p^m)\mu_r + (1+p^m)m\mu_1}{(1+p^m)\mu_r + (1-p^m)m\mu_1}. \tag{A8}$$

2. Detailed derivations for the transformed viscosity

We consider a radial coordinate transformation $r' = F(r,\theta)$ and $\theta' = \theta$ to transform the circular shell with $\boldsymbol{\mu}_s = \mathrm{diag}(\mu_r, \mu_\theta) = \mathrm{diag}(0, \infty)$ into the irregular shaped shell. According to the transformation rule $\boldsymbol{\mu}' = \det \mathbf{J}(\mathbf{J}^{\mathrm{T}})^{-1}\boldsymbol{\mu}\mathbf{J}^{-1}$, the transformed viscosity can be expressed in detail as

$$\boldsymbol{\mu}_s' = \frac{1}{\det \mathbf{J}}\begin{pmatrix} \mu_r\left(\frac{r'\partial\theta'}{r\partial\theta}\right)^2 + \mu_\theta\left(\frac{r'\partial\theta'}{\partial r}\right)^2 & -\mu_r\left(\frac{\partial r'}{r\partial\theta}\right)\left(\frac{r'\partial\theta'}{r\partial\theta}\right) - \mu_\theta\left(\frac{\partial r'}{\partial r}\right)\left(\frac{r'\partial\theta'}{\partial r}\right)\\ -\mu_r\left(\frac{\partial r'}{r\partial\theta}\right)\left(\frac{r'\partial\theta'}{r\partial\theta}\right) - \mu_\theta\left(\frac{\partial r'}{\partial r}\right)\left(\frac{r'\partial\theta'}{\partial r}\right) & \mu_r\left(\frac{\partial r'}{r\partial\theta}\right)^2 + \mu_\theta\left(\frac{\partial r'}{\partial r}\right)^2 \end{pmatrix}. \tag{A9}$$

Since $\mu_r = 0$, $\mu_\theta = \infty$, $\frac{\partial r'}{\partial r}$, and $\frac{\partial r'}{\partial\theta}$ have finite values, $\frac{\partial\theta'}{\partial r} = 0$, and $\frac{\partial\theta'}{\partial\theta} = 1$, we have

$$\begin{aligned}
&\mu_r\left(\frac{r'\partial\theta'}{r\partial\theta}\right)^2 + \mu_\theta\left(\frac{r'\partial\theta'}{\partial r}\right)^2 = 0,\\
&\left[-\mu_r\left(\frac{\partial r'}{r\partial\theta}\right)\left(\frac{r'\partial\theta'}{r\partial\theta}\right) - \mu_\theta\left(\frac{\partial r'}{\partial r}\right)\left(\frac{r'\partial\theta'}{\partial r}\right)\right]\text{is finite},\\
&\mu_r\left(\frac{\partial r'}{r\partial\theta}\right)^2 + \mu_\theta\left(\frac{\partial r'}{\partial r}\right)^2 = \infty.
\end{aligned} \tag{A10}$$

Using μ_{11}, μ_{12}, μ_{21}, and μ_{22} to represent the components of $\boldsymbol{\mu}_s'$, we get

$$\boldsymbol{\mu}_s' = \begin{bmatrix}\mu_{11} & \mu_{12}\\ \mu_{21} & \mu_{22}\end{bmatrix}, \quad \Delta \equiv \det \boldsymbol{\mu}_s' = \mu_{11}\mu_{22} - \mu_{12}^2 = \mu_r\mu_\theta\left(\frac{r'\partial\theta'}{r\partial\theta}\frac{\partial r'}{\partial r} + \frac{r'\partial\theta'}{\partial r}\frac{\partial r'}{r\partial\theta}\right)^2 > 0, \tag{A11}$$

where $\mu_{11} = 0$, $\mu_{12} = \mu_{21}$ are finite values dependent on the transformation, and $\mu_{22} = \infty$. By substituting Eq. (A11) into $\nabla \cdot (\gamma \nabla P) = 0$, we write the Laplace equation in cylindrical coordinates as

$$\nabla \cdot (\boldsymbol{\gamma}\nabla P) = \frac{1}{r}\frac{\partial}{\partial r}\left[r\left(\gamma_{rr}\frac{\partial P}{\partial r} + \gamma_{r\theta}\frac{1}{r}\frac{\partial P}{\partial\theta}\right)\right] + \frac{1}{r}\frac{\partial}{\partial\theta}\left[\gamma_{r\theta}\frac{\partial P}{\partial r} + \gamma_{\theta\theta}\frac{1}{r}\frac{\partial P}{\partial\theta}\right] = 0, \tag{A12}$$

where

$$\boldsymbol{\gamma} = \frac{h^3}{12}\boldsymbol{\mu}_s'^{-1} = \frac{h^3}{12\Delta}\begin{pmatrix}\mu_{22} & -\mu_{12}\\ -\mu_{12} & \mu_{11}\end{pmatrix}. \tag{A13}$$

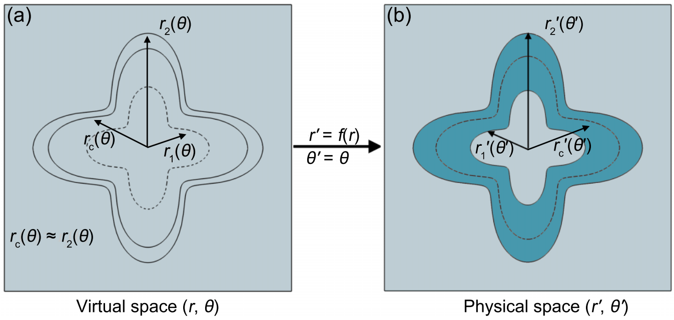

FIG. 11. Diagram of the concentrating coordinate transformation. Null medium requires that $r_c(\theta) \approx r_2(\theta)$.

Here, we define

$$\frac{1}{\Delta}\begin{pmatrix} \mu_{22} & -\mu_{12} \\ -\mu_{12} & \mu_{11} \end{pmatrix} \equiv \begin{pmatrix} \gamma_{rr} & \gamma_{r\theta} \\ \gamma_{r\theta} & \gamma_{\theta\theta} \end{pmatrix}. \tag{A14}$$

We consider the singular limit

$$\mu_{11} = \varepsilon, \quad \mu_{22} = \frac{M}{\varepsilon}, \quad \mu_{12} = \text{finite}, \quad \varepsilon \to 0^+, \quad M > 0, \tag{A15}$$

so that

$$\Delta = \mu_{11}\mu_{22} - \mu_{12}^2 = M - \mu_{12}^2 \equiv D > 0, \tag{A16}$$

and the elements of $\boldsymbol{\gamma}$ scale as

$$\gamma_{rr} = \frac{\mu_{22}}{\Delta} = O(\varepsilon^{-1}), \quad \gamma_{r\theta} = -\frac{\mu_{12}}{\Delta} = O(1), \quad \gamma_{\theta\theta} = \frac{\mu_{11}}{\Delta} = O(\varepsilon). \tag{A17}$$

For clarity, we rewrite Eq. (A12) by extracting the leading divergent part,

$$\nabla \cdot (\boldsymbol{\gamma}\nabla P) = \gamma_{rr}A[P] + B[P], \tag{A18}$$

where

$$A[P] = \frac{1}{r}\frac{\partial}{\partial r}\left(r\frac{\partial P}{\partial r}\right) + \frac{1}{\gamma_{rr}}\frac{\partial \gamma_{rr}}{\partial r}\frac{\partial P}{\partial r} = O(1), \tag{A19}$$

$$B[P] = \frac{1}{\gamma_{rr}}\frac{1}{r}\frac{\partial}{\partial r}\left[r\gamma_{r\theta}\frac{1}{r}\frac{\partial P}{\partial \theta}\right] + \frac{1}{\gamma_{rr}}\frac{1}{r}\frac{\partial}{\partial \theta}\left[\gamma_{r\theta}\frac{\partial P}{\partial r} + \gamma_{\theta\theta}\frac{1}{r}\frac{\partial P}{\partial \theta}\right] = O(\varepsilon). \tag{A20}$$

Therefore, $B[P] = O(\varepsilon)$ is negligible compared to the divergent leading term $\gamma_{rr}A[P] = O(\varepsilon^{-1})$. In the singular limit $\mu_{11} \to 0$, $\mu_{22} \to \infty$, the components involving μ_{12} are parametrically suppressed in the equation, and we can safely omit (or set $\mu_{12} = 0$) without incurring any divergence or loss of generality at leading order. The divergent behavior is governed entirely by the γ_{rr} term, unrelated to μ_{12}. In conclusion, the off-diagonal components of $\boldsymbol{\mu}_s'$ have negligible effects on transport and can thus be omitted. By setting them to zero, the simplified $\boldsymbol{\mu}_s'$ becomes

$$\boldsymbol{\mu}_s' = \text{diag}(0, \infty). \tag{A21}$$

3. Proof from the view of a null medium

From the perspective of a null medium, we theoretically analyze that a metashell with extreme viscosity anisotropy exhibits self-adaptive and free-form properties. Figures 11(a) and 11(b) provide a schematic illustration of the coordinate transformation for concentration. In virtual space, the viscosity is isotropic and homogeneous with μ_b. The concentrator is described by three irregularly shaped contours: $r_2(\theta)$, $r_c(\theta)$, and $r_1(\theta)$. We compress the larger region $r < r_c(\theta)$ into a smaller region $r' < r_1'(\theta')$ and stretch the shell region $r_c(\theta) < r < r_2(\theta)$ into the shell region $r_1'(\theta') < r' < r_2'(\theta')$. The corresponding transformation can be expressed as

$$r' = \frac{r_1(\theta)}{r_c(\theta)}r, \quad r < r_c(\theta), \tag{A22a}$$

$$r' = \frac{[r_2(\theta) - r_1(\theta)]r}{r_2(\theta) - r_c(\theta)} + \frac{[r_1(\theta) - r_c(\theta)]r_2(\theta)}{r_2(\theta) - r_c(\theta)}, \quad r_c(\theta) < r < r_2(\theta), \tag{A22b}$$

$$\theta' = \theta. \tag{A22c}$$

Here, we consider that the three contours share the same shape factor $r(\theta)$, such that $r_2(\theta) = \omega_2 r(\theta)$, $r_c(\theta) = \omega_c r(\theta)$, and $r_1(\theta) = \omega_1 r(\theta)$, where $r(\theta)$ is an arbitrary continuous function with a period of 2π. The constants ω_2, ω_c, and ω_1 satisfy the condition $\omega_1 < \omega_c < \omega_2$. The null medium condition requires that $r_c(\theta) \approx r_2(\theta)$, as shown in Fig. 11(a). In other words, $\omega_c \approx \omega_2$. Under these conditions, we derive the transformed viscosity in the shell region as

$$\boldsymbol{\mu}_s' = \mu_b \begin{bmatrix} \mu_\alpha & \mu_\beta \\ \mu_\beta & \mu_\zeta \end{bmatrix}, \tag{A23}$$

where the components are

$$\mu_\alpha = \frac{(\omega_2 - \omega_c)r'}{(\omega_2 - \omega_c)r' - \omega_2(\omega_1 - \omega_c)r(\theta)}, \quad \mu_\beta = -\frac{\omega_2(\omega_1 - \omega_c)[dr(\theta)/d\theta]}{\omega_2 - \omega_1},$$
$$\mu_\zeta = \frac{(\omega_2 - \omega_c)r' - \omega_2(\omega_1 - \omega_c)r(\theta)}{(\omega_2 - \omega_c)r'} + \frac{\omega_2^2(\omega_c - \omega_1)^2[dr(\theta)/d\theta]^2[(\omega_2 - \omega_c)r' - \omega_2(\omega_1 - \omega_c)r(\theta)]}{(\omega_2 - \omega_1)^2(\omega_2 - \omega_c)r'}. \tag{A24}$$

Since a null medium requires that $\omega_2 \approx \omega_c$, the diagonal components can be simplified as

$$\mu_\alpha = \delta, \quad \mu_\zeta = \tfrac{1}{\delta}, \tag{A25}$$

where $\delta \approx 0$. Therefore, we obtain the transformed viscosity of the metashell as

$$\boldsymbol{\mu}_s' = \begin{bmatrix} 0 & \mu_b\mu_\beta \\ \mu_b\mu_\beta & \infty \end{bmatrix}. \tag{A26}$$

Since μ_b and μ_β are finite values, Eq. (A26) has the same form as Eq. (A11). According to the theoretical analysis in the main text, the exact values of μ_b and μ_β are nonessential because the off-diagonal components of $\boldsymbol{\mu}_s'$ have little effect on transport. By setting μ_β as zero and μ_b as an arbitrary finite value, we get the transformed viscosity of the shell, that is,

$$\boldsymbol{\mu}_s' = \begin{bmatrix} 0 & 0 \\ 0 & \infty \end{bmatrix}, \tag{A27}$$

which means that metashells with extreme viscosity anisotropy exhibit both environmental adaptability and geometric freedom, consistent with the conclusion in the main text.

APPENDIX B: QUANTITATIVE ANALYSIS OF SIMULATION RESULTS

1. Detailed velocity differences in 2D simulations

The velocity distributions for the reference groups and the detailed velocity differences between v_m and v_r are shown in Figs. 12(a)–12(f). Figure 12(a) shows the velocity distribution of the reference group when $\mu_b = \mu_f$, with the velocity being approximately 4.4×10^{-4} m/s. We then extract velocity data along four horizontal lines at $y = 0, 3, 6, 9$ cm and plot them in Fig. 12(b). The

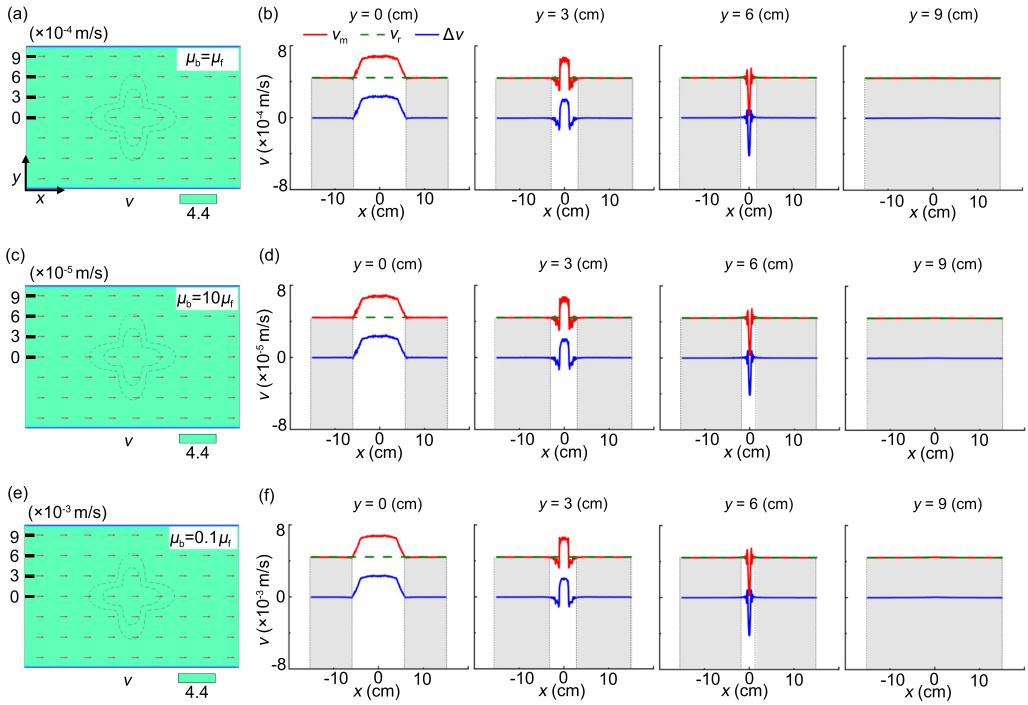

FIG. 12. (a) Velocity distribution of the reference group when $\mu_b = \mu_f$. (b) Velocity data of (a) along four horizontal lines at $y = 0, 3, 6, 9\,\mathrm{cm}$. (c), (e) Velocity distribution when $\mu_b = 10\mu_f$, and $0.1\mu_f$, respectively. (d), (f) Velocity data of (c) and (e) along four horizontal lines at $y = 0, 3, 6, 9\,\mathrm{cm}$, respectively.

red lines represent the velocity of the metashell, v_m, the green dashed lines represent the reference velocity, v_r, and the blue lines at the bottom indicate the velocity differences, $\Delta v = v_m - v_r$. The gray regions correspond to region III. It is observed that $\Delta v = 0$ in region III, confirming that the metashell has no impact on the background velocity field. This result holds for background viscosities of $\mu_b = 10\mu_f$ and $\mu_b = 0.1\mu_f$, as shown in Figs. 12(c)–12(f).

2. Detailed quantitative analyses in 3D simulations

We present detailed quantitative analyses of the 3D simulations. Figure 13(a) is the pressure distribution. The straight isobars confirm the accuracy of our design. We test the metashell's self-adaptability by modifying the environmental structure. By keeping the liquid material unchanged, we alter the structure of the background region to effectively adjust the viscosity of the liquid, as shown in Fig. 13(b). The straight isobars confirm that the metashell remains invisible, demonstrating its ability to adapt to changes in the background structure. To further quantify, we read the pressure data along the outer contour of the metashell at the $z = 0.01\,\mathrm{cm}$ plane and compared them with the reference groups. Figures 13(c) and 13(d) show the comparison results, where the two sets of data overlap, confirming the accuracy. We also extracted the pressure data at the $z = 0.01\,\mathrm{cm}$ plane for two different backgrounds to observe the pressure distribution. As shown in Figs. 13(e) and 13(f), the pressure in region III follows a linear distribution, while each section of the metashell approximates an isobaric region. Figures 13(g) and 13(h) further illustrate the pressure distribution along the $y = 0\,\mathrm{cm}$ line on this plane under different backgrounds. It can be seen that under both background conditions, the metashell region is nearly isobaric, and the pressure in region III overlaps with the reference group data. Moreover, the pressure gradient in region I is greater than that in region III, further validating the accuracy of the theory.

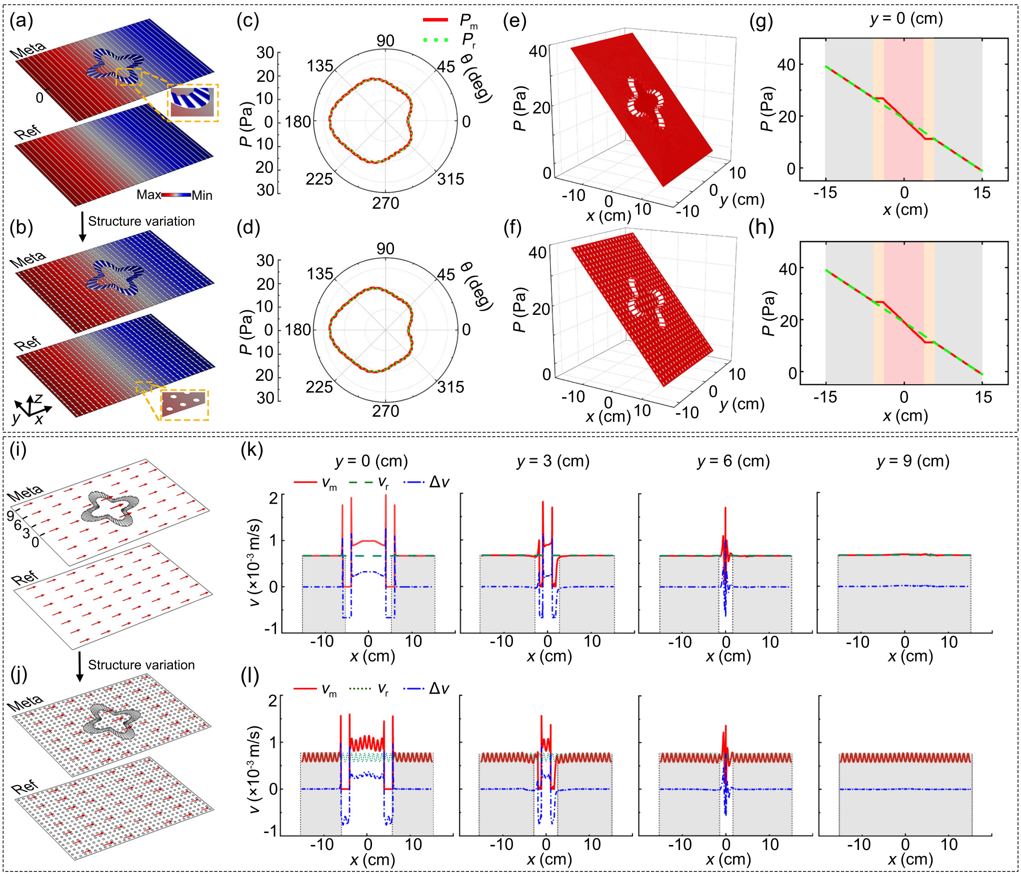

FIG. 13. 3D simulation results of the metashell. (a), (b) Pressure distributions of the metashell and reference groups under two different backgrounds. (c)–(l) Extracted results at the $z = 0.01$ cm plane. (c), (d) Pressure profiles along the outer contour of the shell for the metashell (P_m, red solid) and reference (P_r, green dotted). (e), (f) Pressure profiles for the metashell. (g), (h) Pressure profiles along $y = 0$, where pink and gray areas denote regions I and III, respectively. (i), (j) Velocity distributions with normalized vectors (red arrows). (k), (l) Velocity profiles along $y = 0, 3, 6, 9$ cm comparing the metashell (v_m, red solid), reference (v_r, green dashed), and their difference (Δv, blue dotted). Gray areas denote region III.

The corresponding velocity distributions are shown in Figs. 13(i) and 13(j). The straight velocity arrow indicates that the metashell has no effect on the velocity in region III but increases the velocity in region I. Similarly, we record the velocity data along four lines at $y = 0, 3, 6,$ and 9 cm at the $z = 0.01$ cm plane, comparing the differences with the reference group to quantify the impact on the background. The blue segments at the bottom of Figs. 13(k) and 13(l) represent these differences, which are zero in region III and greater than zero in region I under both background conditions, confirming the correctness of the model.

3. Simulation results of the shell solely composed of isobaric regions

We perform simulations to show that if the shell region is composed entirely of isobaric regions rather than alternating structures, the background physical field will be disrupted. See Fig. 14. We increase the water height in the whole region of the shell, and we refer to it as an obstacle group. Similarly, we simulate the pressure distributions [Figs. 14(a) and 14(b)] and velocity distributions

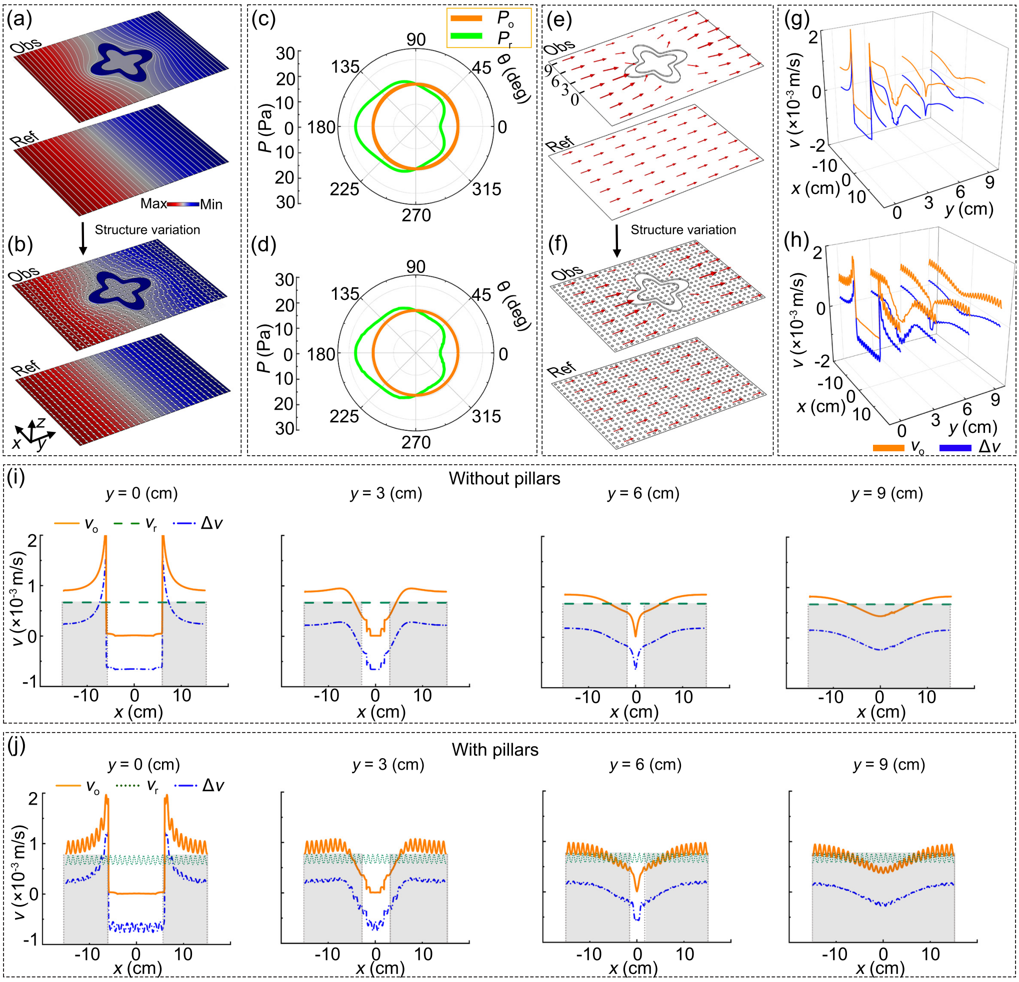

FIG. 14. Simulation results of the shell solely composed of isobaric regions. (a), (b) Pressure distributions of the obstacle (Obs) and reference groups under two different backgrounds. (c), (d) Pressure profiles along the shell's outer contour at the $z = 0.01$ cm plane for the Obs (orange, P_o) and reference (green, P_r) groups. (e), (f) Corresponding velocity distributions, with red arrows denoting normalized velocity vectors. (g), (h) Velocity profiles along four lines ($y = 0, 3, 6, 9$ cm) at the $z = 0.01$ cm plane under both backgrounds. Solid lines indicate the Obs velocity v_o (orange) and the difference $\Delta v = v_o - v_r$ (blue). (i) and (j) Detailed velocity differences under the two backgrounds, where green dashed lines represent the reference velocity v_r.

[Figs. 14(e) and 14(f)] under two different backgrounds, which are the same as that in the main text. It is clear that the background physical field is disrupted. We extract the pressure data along the outer contour of the shell for both obstacle groups (P_o) and reference groups (P_r) for quantitative comparison, as shown in Figs. 14(c) and 14(d). We can see that the pressure distribution shows significant deviations. Similarly, we extract the velocity data along four lines at $y = 0, 3, 6,$ and 9 cm in the $z = 0.01$ cm plane, and we compare the differences with the reference group to quantify the impact on the background. The results, shown in Figs. 14(g) and 14(h), indicate that the blue segments at the bottom do not equal zero in region III. To see this more clearly, we present the detailed differences between the velocity of the obstacle group (v_o) and the reference group (v_r) under these two different backgrounds. Figures 14(i) and 14(j) are the results corresponding to two

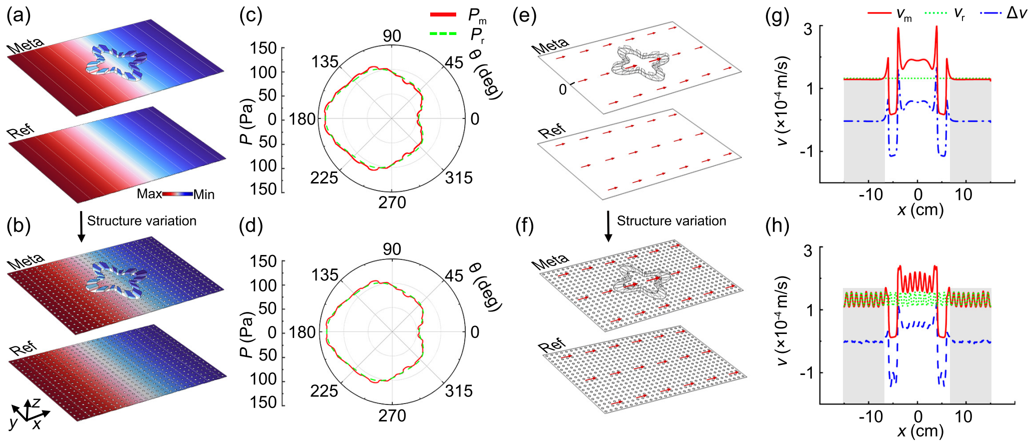

FIG. 15. Simulation results of the actual experimental structure. (a), (b) Pressure distributions of the metashell and reference under two different backgrounds. (c), (d) Pressure profiles along the shell's outer contour at $z = 0.05$ cm for the metashell (P_m, red solid line) and reference (P_r, green dotted line). (e), (f) Corresponding velocity fields (red arrows: normalized velocity). (g), (h) Velocity profiles along $y = 0$ at $z = 0.05$ cm, showing v_m (red solid line), v_r (green dashed line), and their difference Δv (blue dotted line). Gray regions denote region III.

different backgrounds. The blue segments at the bottom represent the differences $\Delta v = v_\mathrm{o} - v_\mathrm{r}$, which are not zero in region III. These results demonstrate that the shell composed entirely of isobaric regions will disrupt the background physical fields.

APPENDIX C: EXPERIMENTAL DETAILS

1. Experimental procedures

To implement the high- and low-pressure boundary conditions for the simulated structure, we add a reservoir at the high-pressure side to maintain the high-pressure boundary while ensuring the entire model is filled with liquid. At the low-pressure side, the liquid naturally flows out. The remaining surfaces, in contact with solid materials, naturally satisfy the no-slip boundary condition. Due to limitations in the experimental process, we relax the structural parameters without affecting the physical conclusions. The channel height of the Hele-Shaw cell is increased from 0.02 to 0.1 cm, and the metashell is divided into 36 parts instead of 72 for demonstration purposes. These adjustments do not affect the physical results but are made to reduce the fabrication difficulty. The simulation results of the actual experimental structure are shown in Fig. 15. We account for gravitational acceleration. Figures 15(a)–15(d) are the pressure distributions under two backgrounds. The invisible performance remains satisfactory. Figures 15(e)–15(h) are the corresponding velocity distributions, which are consistent with what our theoretical model predicts.

2. Quantitative analysis of the experimental streamlines

To quantitatively evaluate the extent to which the streamlines are undisturbed, we extracted spatial data directly from the experimental images in Figs. 7(d) and 7(e). We analyzed all eight visible streamlines. As illustrated in Fig. 16, we established a 2D Cartesian coordinate system mapping the cropped experimental images to a 30 mm × 20 mm bounding box, with the origin (0, 0) at the bottom-left corner. (Note: These dimensional values represent the relative coordinates on the scaled image for calculation purposes, rather than the absolute physical dimensions of the experimental setup.)

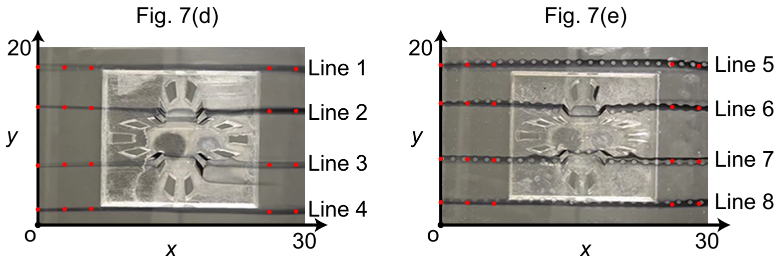

FIG. 16. Data extraction for evaluating streamline straightness. A coordinate system is established for the experimental images from Figs. 7(d) and 7(e). Red dots mark the discrete points sampled along the ink streamlines (lines 1–8) to quantitatively calculate their vertical deviations.

Based on this image-coordinate system, we identified the initial transverse coordinate of each streamline at $x = 0$, and we extracted the coordinates of four representative downstream points ($x = 3, 6, 26, 29$) along the flow direction spanning across the functional region. The extracted raw coordinates (x, y) are as follows:

For Fig. 7(d):

Line 1: $(0, 17.80) \rightarrow (3, 17.70) \rightarrow (6, 17.70) \rightarrow (26, 17.64) \rightarrow (29, 17.57)$,

Line 2: $(0, 13.30) \rightarrow (3, 13.25) \rightarrow (6, 13.17) \rightarrow (26, 12.80) \rightarrow (29, 12.85)$,

Line 3: $(0, 6.70) \rightarrow (3, 6.80) \rightarrow (6, 6.85) \rightarrow (26, 6.75) \rightarrow (29, 6.78)$,

Line 4: $(0, 1.75) \rightarrow (3, 1.78) \rightarrow (6, 1.82) \rightarrow (26, 1.48) \rightarrow (29, 1.53)$.

For Fig. 7(e):

Line 5: $(0, 18.00) \rightarrow (3, 18.05) \rightarrow (6, 18.06) \rightarrow (26, 18.10) \rightarrow (29, 17.90)$,

Line 6: $(0, 13.70) \rightarrow (3, 13.70) \rightarrow (6, 13.65) \rightarrow (26, 13.30) \rightarrow (29, 13.15)$,

Line 7: $(0, 7.45) \rightarrow (3, 7.40) \rightarrow (6, 7.30) \rightarrow (26, 7.20) \rightarrow (29, 7.15)$,

Line 8: $(0, 2.55) \rightarrow (3, 2.50) \rightarrow (6, 2.40) \rightarrow (26, 2.30) \rightarrow (29, 2.40)$.

To quantitatively represent the straightness of the trajectories and eliminate the influence of the image scaling factor, we evaluated two physical metrics for each streamline:

(1) Maximum Absolute Deviation ($|\Delta y|_{\max}$). The maximum transverse spatial shift of the trace's center from its initial position in the image coordinate system.

(2) Deviation Percentage $[(|\Delta y|_{\max}/W_{\mathrm{local}}) \times 100\%]$. The ratio of the maximum deviation to the measured local width (W_{local}) of that specific ink trace in the image. This dimensionless ratio represents the shift relative to the natural diffusion broadening of the ink.

The calculated quantitative data are summarized in Table I.

TABLE I. Quantitative metrics of streamline straightness extracted from the experimental images in Figs. 7(d) and 7(e).

Case	Line no.	W_{local} (mm)	$\lvert\Delta y\rvert_{\max}$ (mm)	Deviation percentage
Fig. 7(d)	Line 1	0.76	0.23	30.3%
	Line 2	0.76	0.50	65.8%
	Line 3	0.60	0.15	25.0%
	Line 4	0.62	0.27	43.6%
Fig. 7(e)	Line 5	0.75	0.10	13.3%
	Line 6	0.72	0.55	76.4%
	Line 7	0.70	0.30	42.9%
	Line 8	0.70	0.25	35.7%

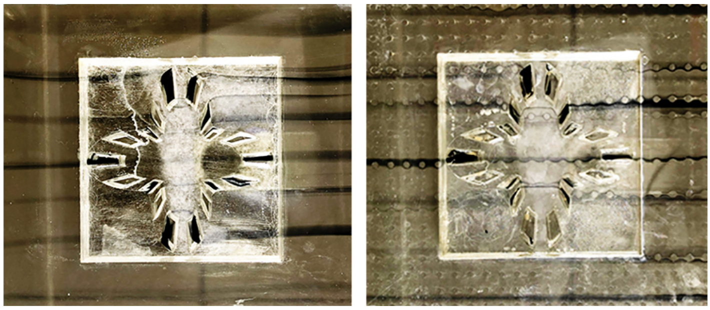

FIG. 17. Photographs of the experimental results for two setups, with the number of streamlines increased from four to seven.

As the Deviation Percentage demonstrates, the maximum spatial deviations for all streamlines are smaller than the ink traces' own natural diffusion widths. This supports the conclusion that the macroscale background velocity field is nearly undisturbed.

3. Additional experiments with seven streamlines

We conducted additional experiments by increasing the number of streamlines from four to seven, thereby enhancing the credibility of our results. The results are shown in Fig. 17. As the result demonstrates, the cloaking effect remains robust with seven streamlines, which substantiates the reliability of our results. It is worth noting that with dye injection, the ink traces inevitably broaden and bifurcate as they flow, and this effect becomes increasingly prominent as the streamline number increases. This is why we initially chose four lines for clarity.

APPENDIX D: POTENTIAL APPLICATIONS

The metashell can locally enhance the flow velocity in target regions while nearly preserving the background flow, offering potential for accelerating liquid mixing within microfluidic chips. Figure 18(a) illustrates a prospective application scenario in a microfluidic chip. The simulation

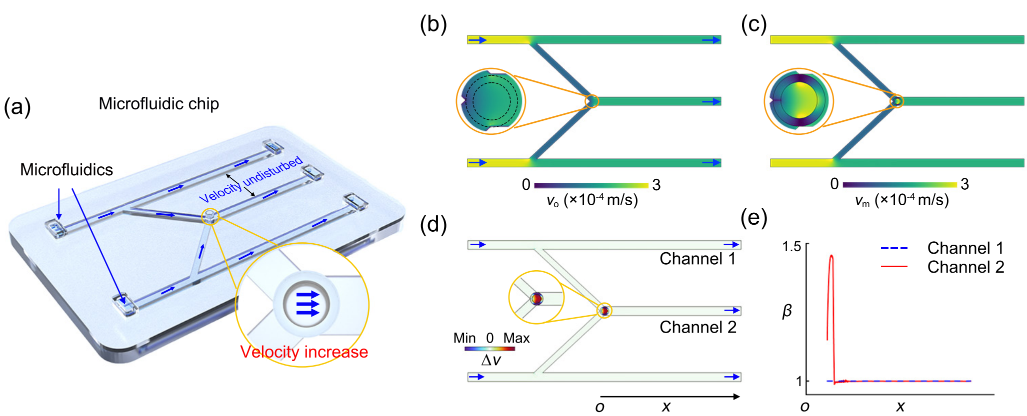

FIG. 18. Potential application of the metashell for microfluidic chips. (a) Schematic diagram of the microfluidic chip. (b) Velocity distribution without the metashell in the microfluidic chip. (c) Velocity distribution with the metashell in the microfluidic chip. (d) The velocity difference Δv after introducing the metashell. (e) The velocity ratio β for channel 1 and channel 2 vs x.

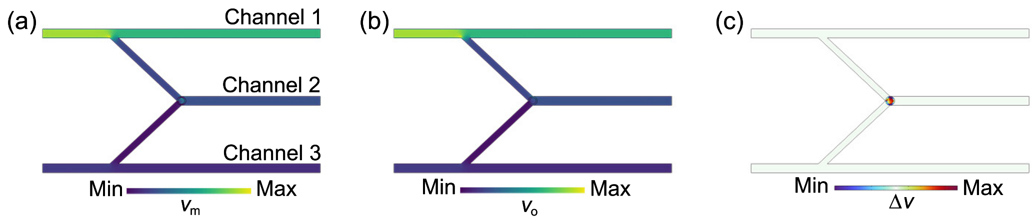

FIG. 19. Simulation results for mixing liquids with different viscosities. (a) Velocity distribution of the metashell (v_{m}). (b) Velocity distribution of the original background without the metashell (v_{o}). (c) The velocity difference ($\Delta v = v_{\mathrm{m}} - v_{\mathrm{o}}$).

domain is 3.2 cm $\times$ 6.2 cm with a channel width of 2 mm. The metashell is placed in the middle channel to accelerate the mixing of liquids flowing from the other two channels within the shell region. Figure 18(b) is the velocity distribution of the original background without a metashell, denoted as v_{o}. The left two boundaries are set to 40 Pa as high pressure, and the right three boundaries are set to 0 Pa as low pressure. We maintain the boundary conditions unchanged and introduce the metashell into channel 2. The velocity distribution, denoted as v_{m}, is shown in Fig. 18(c). Comparing Figs. 18(b) and 18(c), we observe an increase in velocity in the central region of the metashell, while the velocity outside the metashell remains undisturbed. For further quantitative analysis, we define $\Delta v = v_{\mathrm{m}} - v_{\mathrm{o}}$ and plot the distribution of Δv as shown in Fig. 18(d). We observe that the velocity difference inside the metashell region is greater than zero, while that in the exterior region is zero, which validates the prediction. Furthermore, we extracted velocity data along the x-direction in channels 1 and 2 and defined $\beta = v_{\mathrm{m}}/v_{\mathrm{o}}$, as shown in Fig. 18(e). The result quantitatively shows that the velocity in the metashell's core region increases, whereas velocities in other regions remain undisturbed.

To further demonstrate its environment-adaptive nature, we simulated the metadevice in a microfluidic mixer with different viscosities. Theoretically, the extreme effective viscosity tensor of the metashell cancels out background viscosity terms in the governing equations, making the device's performance independent of local fluid properties. To verify this, three distinct liquids (1×10^{-3}, 3×10^{-3}, and 5×10^{-3} Pa s) are injected into the system. As shown in Fig. 19, the flow velocity is accelerated within the core region, which enhances convective mixing. Meanwhile, the background flow outside remains undisturbed ($\Delta v \approx 0$). This confirms that the design robustly concentrates flow and maintains cloaking even for mixing liquids with varying viscosities.

---

[1] S. Battat, D. A. Weitz, and G. M. Whitesides, Nonlinear phenomena in microfluidics, Chem. Rev. **122**, 6921 (2022).

[2] E. K. Sackmann, A. L. Fulton, and D. J. Beebe, The present and future role of microfluidics in biomedical research, Nature (London) **507**, 181 (2014).

[3] H. Chen, C. T. Chan, and P. Sheng, Transformation optics and metamaterials, Nat. Mater. **9**, 387 (2010).

[4] M. Wegener, Metamaterials beyond optics, Science **342**, 939 (2013).

[5] M. Kadic, T. Bückmann, R. Schittny, and M. Wegener, Metamaterials beyond electromagnetism, Rep. Prog. Phys. **76**, 126501 (2013).

[6] Y. A. Urzhumov and D. R. Smith, Fluid flow control with transformation media, Phys. Rev. Lett. **107**, 074501 (2011).

[7] J. Park, J. R. Youn, and Y. S. Song, Hydrodynamic metamaterial cloak for drag-free flow, Phys. Rev. Lett. **123**, 074502 (2019).

[8] E. Boyko, V. Bacheva, M. Eigenbrod, F. Paratore, A. D. Gat, S. Hardt, and M. Bercovici, Microscale hydrodynamic cloaking and shielding via electro-osmosis, Phys. Rev. Lett. **126**, 184502 (2021).

[9] F. Tay, Y. Zhang, H. Xu, H. Goh, Y. Luo, and B. Zhang, A metamaterial-free fluid-flow cloak, Natl. Sci. Rev. **9**, nwab205 (2022).

[10] M. Chen, X. Shen, and L. Xu, Realizing the thinnest hydrodynamic cloak in porous medium flow, The Innovation **3**, 100263 (2022).

[11] G. Dai and J. Wang, Transformation hydrodynamic metamaterials: Rigorous arguments on form invariance and structural design with spatial variance, Phys. Rev. E **107**, 055108 (2023).

[12] J. Park, J. R. Youn, and Y. S. Song, Metamaterial hydrodynamic flow concentrator, Extreme Mech. Lett. **42**, 101061 (2021).

[13] J. Park, J. R. Youn, and Y. S. Song, Fluid-flow rotator based on hydrodynamic metamaterial, Phys. Rev. Appl. **12**, 061002(R) (2019).

[14] M. Chen, X. Shen, Z. Chen, J. H. Y. Lo, Y. Liu, X. Xu, Y. Wu, and L. Xu, Realizing the multifunctional metamaterial for fluid flow in a porous medium, Proc. Natl. Acad. Sci. USA **119**, e2207630119 (2022).

[15] C. Jiang, H. Nie, M. Chen, X. Shen, and L. Xu, Achieving environmentally-adaptive and multifunctional hydrodynamic metamaterials through active control, Adv. Mater. **37**, 2313986 (2025).

[16] C. Li, L. Xu, L. Zhu, S. Zou, Q. H. Liu, Z. Wang, and H. Chen, Concentrators for water waves, Phys. Rev. Lett. **121**, 104501 (2018).

[17] S. Zou, Y. Xu, R. Zatianina, C. Li, X. Liang, L. Zhu, Y. Zhang, G. Liu, Q. H. Liu, H. Chen, and Z. Wang, Broadband waveguide cloak for water waves, Phys. Rev. Lett. **123**, 074501 (2019).

[18] L. Han, S. Chen, and H. Chen, Water wave polaritons, Phys. Rev. Lett. **128**, 204501 (2022).

[19] M. Chen, X. Shen, G. Zhu, and B. Li, Rapidly achieving uniform flow with a hydrodynamic metadevice, Phys. Fluids **36**, 053611 (2024).

[20] L.-P. Euvé, K. Pham, P. Petitjeans, V. Pagneux, and A. Maurel, Experimental demonstration of negative refraction of water waves using metamaterials with hyperbolic dispersion, Phys. Rev. Fluids **9**, L112801 (2024).

[21] Y. Li, Y. Zhou, Y. Wang, W. Jiang, F. Yang, P. Jin, and J. Huang, Invisible hydrodynamic sensing via metamaterial shells optimized by machine learning, Adv. Mater. **38**, e19721 (2026).

[22] H. Stone, A. Stroock, and A. Ajdari, Engineering flows in small devices: Microfluidics toward a lab-on-a-chip, Annu. Rev. Fluid Mech. **36**, 381 (2004).

[23] R. L. Panton, *Incompressible Flow* (Wiley, New York, 2013).

[24] U. Leonhardt, Optical conformal mapping, Science **312**, 1777 (2006).

[25] J. B. Pendry, D. Schurig, and D. R. Smith, Controlling electromagnetic fields, Science **312**, 1780 (2006).

[26] S. A. Cummer, B.-I. Popa, D. Schurig, D. R. Smith, J. B. Pendry, M. Rahm, and A. Starr, Scattering theory derivation of a 3D acoustic cloaking shell, Phys. Rev. Lett. **100**, 024301 (2008).

[27] A. Alù and N. Engheta, Cloaking a sensor, Phys. Rev. Lett. **102**, 233901 (2009).

[28] T. Han, X. Bai, D. Gao, J. T. L. Thong, B. Li, and C.-W. Qiu, Experimental demonstration of a bilayer thermal cloak, Phys. Rev. Lett. **112**, 054302 (2014).

[29] N. I. Zheludev and Y. S. Kivshar, From metamaterials to metadevices, Nat. Mater. **11**, 917 (2012).

[30] F. Yang, Z. Zhang, L. Xu, Z. Liu, P. Jin, P. Zhuang, M. Lei, J. Liu, J.-H. Jiang, X. Ouyang, F. Marchesoni, and J. Huang, Controlling mass and energy diffusion with metamaterials, Rev. Mod. Phys. **96**, 015002 (2024).

[31] Z. Liu, P. Jin, M. Lei, C. Wang, F. Marchesoni, J.-H. Jiang, and J. Huang, Topological thermal transport, Nat. Rev. Phys. **6**, 554 (2024).

[32] Z. Liu, P. Jin, M. Lei, C. Wang, P. Zhuang, P. Tan, J.-H. Jiang, F. Marchesoni, and J. Huang, Topology in thermal, particle, and plasma diffusion metamaterials, Chem. Rev. **125**, 8655 (2025).

[33] M. Chen, X. Shen, and L. Xu, Hydrodynamic metamaterials: Principles, experiments, and applications, Droplet **2**, e79 (2023).

[34] L. Xu, S. Yang, and J. Huang, Passive metashells with adaptive thermal conductivities: Chameleonlike behavior and its origin, Phys. Rev. Appl. **11**, 054071 (2019).

[35] L. Xu and J. Huang, Chameleonlike metashells in microfluidics: A passive approach to adaptive responses, Sci. China Phys. Mech. Astron. **63**, 228711 (2020).

[36] F. Yang, B. Tian, L. Xu, and J. Huang, Experimental demonstration of thermal chameleonlike rotators with transformation-invariant metamaterials, Phys. Rev. Appl. **14**, 054024 (2020).

[37] Z. Zhang, F. Yang, and J. Huang, Intelligent chameleonlike metashells for mass diffusion, Phys. Rev. Appl. **19**, 024009 (2023).

[38] Y. Huang, J. Zhang, Q. Yang, L. Meng, T. Yang, C.-W. Qiu, and Y. Luo, Transformation-invariant Laplacian metadevices robust to environmental variation, Adv. Mater. **37**, 2412929 (2025).

[39] F. Sun, Y. Liu, Y. Yang, Z. Chen, and S. He, Thermal surface transformation and its applications to heat flux manipulations, Opt. Express **27**, 33757 (2019).

[40] H. B. Sedeh, M. Hosein Fakheri, A. Abdolali, F. Sun, and Y. Ma, Feasible thermodynamics devices enabled by thermal-null medium, Phys. Rev. Appl. **14**, 064034 (2020).

[41] H. Chen, F. Sun, B. Wang, Y. Liu, Z. Chen, and Y. Yang, Thermal camouflages based on 3D thermal-null medium, Int. J. Therm. Sci. **176**, 107506 (2022).

[42] M. H. Fakheri, A. Abdolali, and H. B. Sedeh, Arbitrary shaped acoustic concentrators enabled by null media, Phys. Rev. Appl. **13**, 034004 (2020).

[43] F. Paratore, V. Bacheva, M. Bercovici, and G. V. Kaigala, Reconfigurable microfluidics, Nat. Rev. Chem. **6**, 70 (2022).

[44] T. Moragues, D. Arguijo, T. Beneyton, C. Modavi, K. Simutis, A. R. Abate, J.-C. Baret, A. J. deMello, D. Densmore, and A. D. Griffiths, Droplet-based microfluidics, Nat. Rev. Methods Primers **3**, 32 (2023).

[45] F. Irgens, *Rheology and non-Newtonian Fluids* (Springer, Cham, Switzerland, 2014), Vol. 190.

[46] B. Reyes, A. A. Howard, P. Perdikaris, and A. M. Tartakovsky, Learning unknown physics of non-Newtonian fluids, Phys. Rev. Fluids **6**, 073301 (2021).

[47] L. Talon, Minimum principle for the flow of inelastic non-Newtonian fluids in macroscopic heterogeneous porous media, Phys. Rev. Fluids **7**, L042101 (2022).

[48] Y. Qiu, G. Dai, and J. Huang, Gradient-field-dependent transformation theory: Metamaterial cloaks of non-Newtonian fluids, Phys. Rev. Appl. **23**, 064007 (2025).

[49] W.-S. Yeung, V.-P. Mai, and R.-J. Yang, Cloaking: Controlling thermal and hydrodynamic fields simultaneously, Phys. Rev. Appl. **13**, 064030 (2020).

[50] G. Dai, Y. Zhou, J. Wang, F. Yang, T. Qu, and J. Huang, Convective cloak in Hele-Shaw cells with bilayer structures: Hiding objects from heat and fluid motion simultaneously, Phys. Rev. Appl. **17**, 044006 (2022).

[51] G. Dai and J. Wang, On transformation form-invariance in thermal convection, Materials **16**, 376 (2023).

[52] P. Jin, J. Liu, L. Xu, J. Wang, X. Ouyang, J.-H. Jiang, and J. Huang, Tunable liquid-solid hybrid thermal metamaterials with a topology transition, Proc. Natl. Acad. Sci. USA **120**, e2217068120 (2023).